J. Space Weather Space Clim. 2025, **15**, 44

https://doi.org/10.1051/swsc/2025039

JSWSC

Available online at:
www.swsc-journal.org

TECHNICAL ARTICLE OPEN ACCESS

Improving the global Total Electron Content maps provided by the Ionosphere Monitoring and Prediction Center – preliminary results

Erik Schmölter*, Youssef Tagargouste, Volker Wilken, Martin Kriegel, and Jens Berdermann

Institute for Solar-Terrestrial Physics, German Aerospace Center (DLR), Kalkhorstweg 53, 17235 Neustrelitz, Germany

Received 12 February 2025 / Accepted 18 September 2025

Abstract – Total electron content (TEC) maps are essential for understanding the temporal and spatial variability of the ionosphere, which is of particular importance during the current solar cycle with its multitude of extreme space weather events. This study presents an improved method for the global TEC map of the Ionosphere Monitoring and Prediction Center (IMPC) by incorporating an algorithm based on radial basis function interpolation. By refining the generation of the global TEC map, the accuracy and granularity of ionospheric gradients, which occur during these events, are significantly improved. The validation through comprehensive comparisons with the established TEC map and the global TEC map of the Technical University of Catalonia (UPC) confirms that the new algorithm outperforms previous results. Thus, a more robust framework for ionospheric research and application is provided. TEC gradients derived from the improved TEC maps are important for understanding the space weather impact on Global Navigation Satellite System (GNSS) applications. The new results can support these with more reliable and consistent predictions by accurately capturing these gradients.

Keywords: Space weather / Ionosphere / Monitoring

1 Introduction

Total electron content (TEC) maps are an important space weather monitoring tool and provide information of ionospheric variability (Jakowski et al., 2011b), which can significantly impact the performance of communication (Bust et al., 2021) and navigation (Sreeja, 2016; Coster & Yizengaw, 2021; Demyanov et al., 2022) services. As a result of these impacts, many parts of our modern technological infrastructure, including for example aviation (Kauristie et al., 2021) or satellites (Doornbos & Klinkrad, 2006), are affected by space weather and require ionospheric information based on TEC maps. Ionospheric variations observed with TEC are closely related to solar and geomagnetic activity (Feng et al., 2023) and strong disturbances occur during extreme space weather (Berdermann et al., 2018; Blagoveshchensky et al., 2018). Real-time monitoring and forecast of these conditions help mitigate the risk for our technological infrastructure and reduce the economic impact (Hapgood, 2018).

The Ionosphere Monitoring and Prediction Center (IMPC) operated by the German Aerospace Center (DLR) provides various products focused on monitoring and forecasting the ionospheric state. Ground- and satellite-based measurements are assimilated into models, enabling global predictions in high temporal and spatial resolution (Jakowski et al., 2011b). This allows an assessment of possible space weather impacts on communication and navigation services (Minkwitz et al., 2014; Kriegel & Berdermann, 2020). The global near-real-time TEC map (referenced as SCM in the present study due to the applied successive corrections method) is a crucial product for space weather services (e.g., Space Weather Service Network developed within the Space Safety Programme by the European Space Agency) and used in research.

Ongoing development and validation against the TEC maps of other data providers and independent measurements ensure reliable predictions and trigger improvements to the algorithm if needed (Hoque et al., 2022). The current solar cycle, with the multitude of extreme space weather events (Fang et al., 2022; Themens et al., 2024), has led to a continuous discussion of the TEC map performance, and additional requirements were identified. These are addressed with the algorithm based on radial basis function (RBF) interpolation presented in this study, which differs in two key aspects from the existing approach and thus requires substantial adjustments with impact on the global

*Corresponding author: Erik.Schmoelter@dlr.de

consistency of the TEC map and characteristics of gradients. These gradients occur under varying space weather conditions and complicate statistical analyses or use in applications. An alternative product is presented (referenced as RBF in the present study), which is more appropriate for long-term analyses (i.e., highlighting significant variations), disturbance identification (i.e., ionospheric storm), and recent ionospheric research objectives.

Especially, the details of rapid and localized ionospheric variations are not sufficiently captured by existing global TEC maps, which are commonly used in applications and research. Therefore, developing and validating TEC maps with higher temporal and spatial resolution based on new algorithms is crucial to achieve the desired improvements. The gradients in the TEC maps are intended not only to be corrected using the RBF interpolation (e.g., spatial distribution) but also to be tracked more accurately with both temporal and spatial variability. As a result, the performance of the IMPC TEC map should fulfill current requirements and be competitive or better than products by other institutions in the long term.

The first part of this study introduces the RBF algorithm and the RBF TEC map. The second part presents the validation of the RBF TEC map throughout 2023 with annual, monthly, and daily comparisons. The advantages and disadvantages with regard to the increased requirements are discussed for both, SCM and RBF TEC map. Finally, an outlook is given on the integration of the RBF TEC map as a product in IMPC.

2 Data

IMPC provides a global TEC map, which describes the integrated plasma density of the ionosphere as a regular grid of 2.5° × 5.0° (Kriegel & Berdermann, 2020). The map is generated based on ground-based Global Navigation Satellite Systems (GNSS) measurements. These are provided by several networks of geodetic GNSS receivers, e.g. the International GNSS Service (IGS), and transmitted to the IMPC via the Networked Transport of Radio Technical Commission for Maritime Services (RTCM) via Internet Protocol (NTRIP) developed by the Federal Agency for Cartography and Geodesy (BKG).

The TEC calibration process converts relative TEC from high-rate GNSS measurements into absolute TEC through several processing steps. These include smoothing the code-derived relative TEC using the low-noise, carrier phase-based relative TEC, detecting cycle slips, and estimating instrumental biases at both the receiver and the satellites. The bias estimation is performed by solving a weighted least squares (WLS) system, using the Neustrelitz Total Electron Content Model (NTCM) as a background model (Jakowski et al., 2011b, a).

The calibrated slant TEC at ionospheric piercing points (IPP) are mapped to vertical TEC and assimilated into NTCM according to the algorithm by Jakowski et al. (2011b) to generate the global TEC map. TEC maps are calculated every 5 minutes with a latency of about 2 min to real-time and are available via the IMPC web page.[1]

The RBF algorithm presented in this study requires the NTCM model coefficients and the calibrated vertical TEC measurements at the IPP, which are also used to generate the SCM TEC map (Kriegel & Berdermann, 2020).

The global TEC map of the Technical University of Catalonia (UPC) is used as reference data set against which the RBF and SCM TEC maps are validated. The UPC TEC map is appropriate for this because its performance was validated several times (Orús et al., 2002, 2003; Roma-Dollase et al., 2017) and it was frequently used in preceding studies. UPC, as one of the IGS Ionosphere Associate Analysis Center (IAAC) provides a TEC map with a regular grid of 2.5° × 5.0° (Hernández-Pajares et al., 1999, 2009). The map is generated with the Tomographic Ionosphere model software (TOMION), which uses a multilayer voxel model to calculate the integrated plasma density (Hernández-Pajares et al., 1997; Hernández-Pajares et al., 1999). The present study applies the TEC map, which is calculated with splines-based interpolation every 2 h and is available via the Crustal Dynamics Data Information System (CDDIS) web page[2] (Noll, 2010).

While the UPC TEC map and other IGS products are commonly used for their reliability and consistency, there are several motivations for developing the IMPC TEC map. In this study, the improvements are motivated by space weather impact analyses in aviation by IMPC (Schmölter et al., 2025), which require a more accurate representation of ionospheric gradients and therefore a higher temporal (5 min) and spatial (grid of 1° × 1°) resolution of TEC maps. In this and other cases, adapting TEC products to meet specific application needs (e.g., Tariq et al., 2019) or to enhance regional models (e.g., Krypiak-Gregorczyk et al., 2017) is of interest and allows alternative approaches within an operational environment. Furthermore, the performance, particularly in terms of spatial and temporal resolution or latency, may also require the development of different TEC maps. For this reason, the UPC TEC map is a good reference for assessing the general quality of the RBF TEC map, including e.g., annual, seasonal, or regional variability. However, this preliminary validation should not be understood as optimizing the TEC map to duplicate existing results. In particular, detailed adjustments can only be performed with independent measurements in future studies, possibly resulting in unique features of the RBF TEC map.

3 RBF TEC map via radial basis function interpolation

The RBF algorithm addresses two problems of the SCM TEC map caused during the assimilation process. In the context of IMPC TEC processing, assimilation refers specifically to the adjustment of the NTCM TEC map with the TEC measurements at the IPP. Offsets between the NTCM and the actual state of the ionosphere are always expected, but can be reduced if measurements are available in a region. However, global coverage with measurements is incomplete (e.g., due to geographical limitations) and interpolations are needed in several

[1] IMPC. 2025. Ionosphere Monitoring and Prediction Center – Products [Data set]. German Aerospace Center (DLR). https://impc.dlr.de/products.

[2] CDDIS. 2025. GNSS Atmospheric Products [Data set]. National Aeronautics and Space Administration (NASA). https://cddis.nasa.gov/archive/gnss/products/ionex/

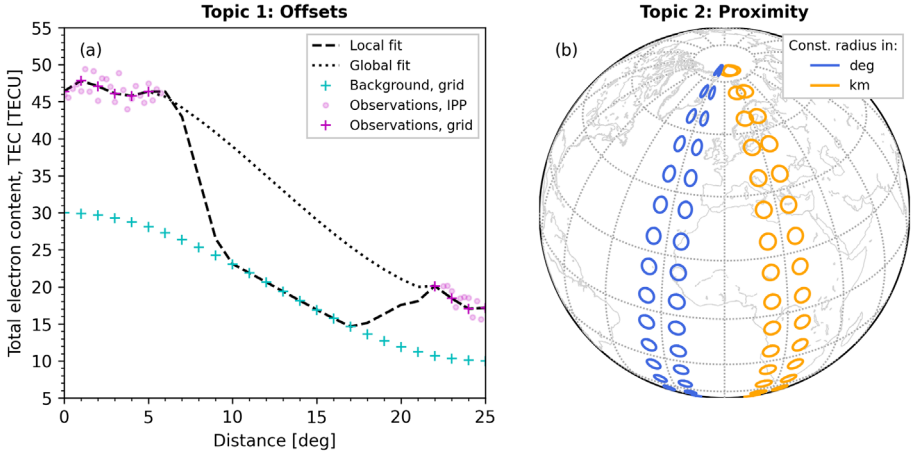

Figure 1. Panel (a) shows an artificial case of TEC measurements in two regions along a slice (magenta) with varying offsets from a background model (cyan). A local (dashed line) and global fit (dotted line) are shown. Panel (b) shows the area covered by circles with constant radius according to spherical (blue) or Cartesian (yellow) coordinates.

regions. Figure 1a presents such a problematic case with two regions of measurements along a slice separated by a measurement gap.

The local fit (dashed line) of measurements and background model causes the result to follow the background model at greater distances from regions with measurements. Transition regions between measurements and the background model are also observed. The SCM TEC map shows this behavior, as the difference at each grid point is calculated with weighted values according to a Gaussian kernel at IPP. This approach creates consistent temporal variations in the different regions, but introduces problems for the analysis of spatial variations. Since the regions with measurements are determined by the GNSS receiver networks, the transition regions in the maps are also stationary and corresponding spatial TEC variations occur. These gradients can dominate spatial analyses (especially long-term) and cannot be addressed by minor adjustments (e.g., increased standard deviation for the Gaussian kernel).

The global fit (dotted line) solves the offset in the region without measurements. For that purpose, the variability of the background model is scaled to fit the measurements. Transition regions should no longer occur with this approach, so that the results are appropriate for spatial analyses and the calculation of gradients. Therefore, the RBF TEC map is adjusted according to this revision.

Figure 2 shows the difference between local and global fit (see Fig. 1a) for two-dimensional data with an artificial example. The TEC measurements in Figure 2a are higher than the background model, which therefore has to be adjusted. The local fit in Figure 2b causes strong gradients in transition regions (see Fig. 2d). Similar features can also be observed in the SCM TEC map under certain space weather conditions. A global fit as intended by the RBF TEC map should improve gradients in these transition regions. This is shown with the example in Figure 2c, which is not impacted by strong gradients (see Fig. 2e).

Figure 1b shows the second feature that is addressed with the RBF algorithm. The assimilation of the SCM TEC map is performed in geographic coordinates, which reduces the process to a two-dimensional problem. The standard deviation for the Gaussian kernel is applied to the spherical distance to estimate the weight of influence related to a grid cell. This ensures equal weight distributions at all latitudes. The RBF TEC map does not require these considerations, as the interpolation is performed in Cartesian coordinates.

There are further considerations for the RBF algorithm, including interpolation at the poles, spatial resolution, and additional filtering. However, these only require minor changes that can be applied to both TEC maps. The RBF algorithm that solves the stated main problems is described below.

Generally, the assimilation is solved with radial basis function (RBF) interpolation, which allows the estimation of values in unstructured data within high-dimensional spaces (Wahba, 1990; Fasshauer, 2007). RBF interpolation was applied in regional TEC models (Mahbuby & Amerian, 2021, 2022) and is an excellent candidate for solving numerical problems in geosciences (Fornberg & Flyer, 2015). The calculation of the RBF interpolation is very resource-intensive (quadratic increase with the number of data points), and 5 min of data contains more than 10,000 IPP. Therefore, the method must be applied with caution.

Figure 3 shows the observed, calibrated values $\mathrm{TEC}_{\mathrm{Obs}}$ as well as the NTCM modeled values $\mathrm{TEC}_{\mathrm{NTCM}}$ at the IPP for an arbitrarily selected period in 2023. The cylindrical equidistant projection in the first row, which is also used for the final map, shows the global distribution of the data. The orthographic projection in the second row better represents the distribution of IPP and is better suited for the steps associated with RBF interpolation (in agreement with the Cartesian coordinate system).

The aim of the approach is to calculate global adjustments for NTCM using RBF interpolation. The base algorithm (Virtanen et al., 2020) must therefore be adjusted to the specific data set. For that purpose, the difference $d\mathrm{TEC}$ of measurements and NTCM model is calculated at all IPP (latitude ϕ and longitude λ) according to

$$d\mathrm{TEC}(\phi,\lambda) = \mathrm{TEC}_{\mathrm{Obs}}(\phi,\lambda) - \mathrm{TEC}_{\mathrm{NTCM}}(\phi,\lambda). \quad (1)$$

These resulting values are projected onto a single layer shell (default heights of 400 km) in Cartesian coordinates. Figure 4a shows the corresponding results for the values from Figure 3.

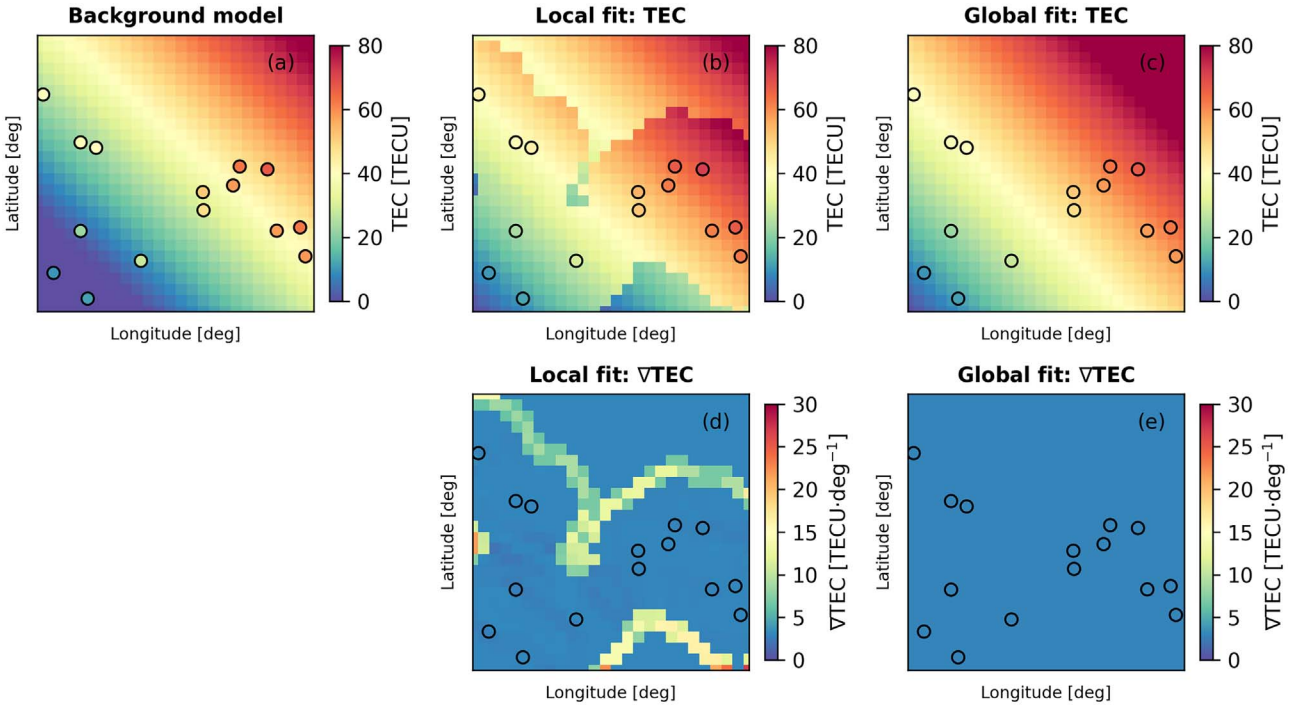

Figure 2. Panel (a) shows an artificial case with the TEC background model (raster) and TEC measurements (filled circles). Panels (b) and (c) show the TEC maps according to a local and global fit, respectively. The bottom panels (d, e) show the corresponding TEC gradients.

The calculated values dTEC and the corresponding locations y define the RBF interpolant f as

$$f(x) = K(x,y)a + P(x)b. \tag{2}$$

The matrix of RBFs $K(x,y)$ centered at the locations y allows to evaluate the locations x according to the distances r with respective RBF $r = \|x - y\|$. The matrix of monomials $P(x)$ ensures convergence (Flyer et al., 2016; Jančič et al., 2021). The coefficients a and b are related according to

$$(K(y,y) + sI)a + P(y)b = d\mathrm{TEC}(y) \tag{3}$$

and

$$P(y)^T a = 0. \tag{4}$$

Solving this system allows us to calculate dTEC at any location x according to the smoothing parameter s (5×10^6, related to scale of coordinates) and an appropriate kernel (linear). Figure 4b shows the RBF interpolated TEC difference $d\mathrm{TEC}_{\mathrm{RBF}}$ from the data in Figure 4a.

The NTCM TEC map is adjusted by adding the RBF interpolant at all grid points of the final map, which is flexible in respect of spatial resolution. The RBF values $\mathrm{TEC}_{\mathrm{RBF}}$ are calculated according to

$$\mathrm{TEC}_{\mathrm{RBF}} = \mathrm{TEC}_{\mathrm{NTCM}} + d\mathrm{TEC}_{\mathrm{RBF}}. \tag{5}$$

The NTCM and RBF TEC map are shown in Figure 5. For the selected period, the RBF TEC map shows significantly higher values, particularly in the ionospheric maximum on the day side (see also Fig. 4b), and the southward trend of the equatorial crest is more pronounced. In regions with a high density of IPP, small-scale variations occur that are particularly noticeable at low TEC values (e.g., on the night side). Whether these variations are real or artifacts must be determined by detailed analysis with independent measurements. If these variations are artifacts, they could be removed using suitable smoothing methods (e.g. median or Gaussian filter). Figure 6 shows the same RBF TEC map in the design for the IMPC.

In addition to the TEC map, an RBF error map is calculated using the RBF algorithm. For this purpose, the IPP data are divided into randomly generated sample data sets. A TEC map is calculated for each sample using the method described. The error is estimated using the standard deviation of this assemble according to

$$\sigma^2 = \frac{1}{N} \sum (\overline{\mathrm{TEC}}_{\mathrm{RBF}} - \mathrm{TEC}_{\mathrm{RBF},i})^2. \tag{6}$$

The number of sample data sets N is set to 5 by default. Figure 7 shows the corresponding TEC error map for the TEC map in Figure 6. For the selected period, two regions are striking (South America and the South Pacific), where the number of IPP is lower, but also stronger TEC variations occur. In addition, both regions coincide with Earth's terminator and the equatorial crest. For these conditions, ionospheric disturbances can be expected (Abdu, 1997; Balan et al., 2018a), which raises the question for future studies whether the error map is also of interest for investigations of such disturbances. The proposed error map complements the established IMPC TEC error map, which estimates the error from the measurements and the error propagation based on the modeling processes.

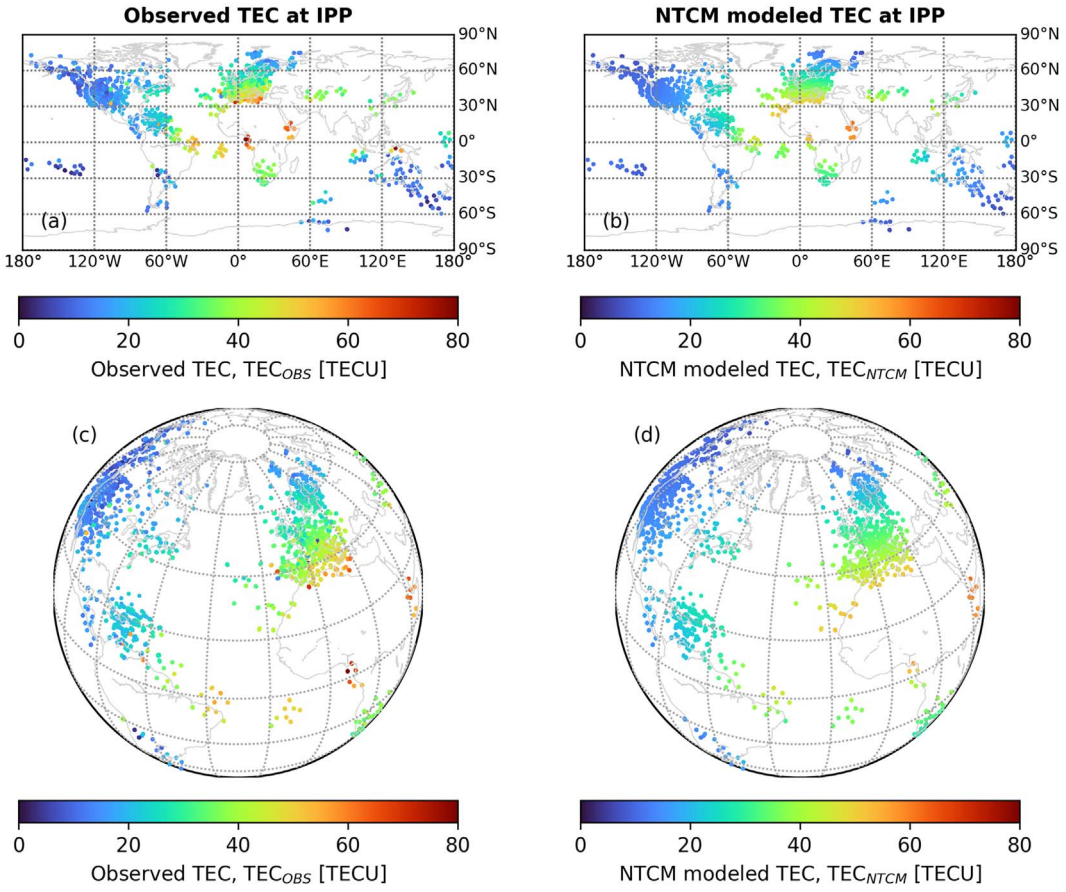

Figure 3. Observed TEC (a, c) and NTCM modeled TEC (b, d) at IPP are shown for 19 May 2023 11:35 UTC. The cylindrical equidistant projection (a, b) corresponds to the target output as a map, while the orthographic projection (c, d) better represents the distribution of IPP for the interpolation.

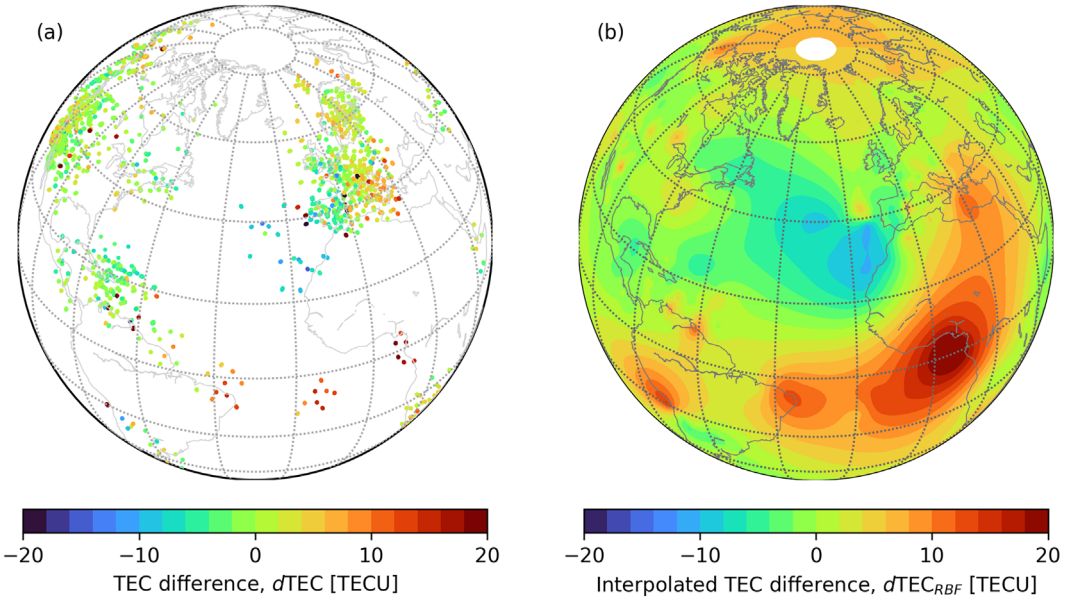

Figure 4. TEC difference between the observed, calibrated values, as well as the NTCM modeled values (a) and the RBF interpolation (b) is shown for 19 May 2023 11:35 UTC.

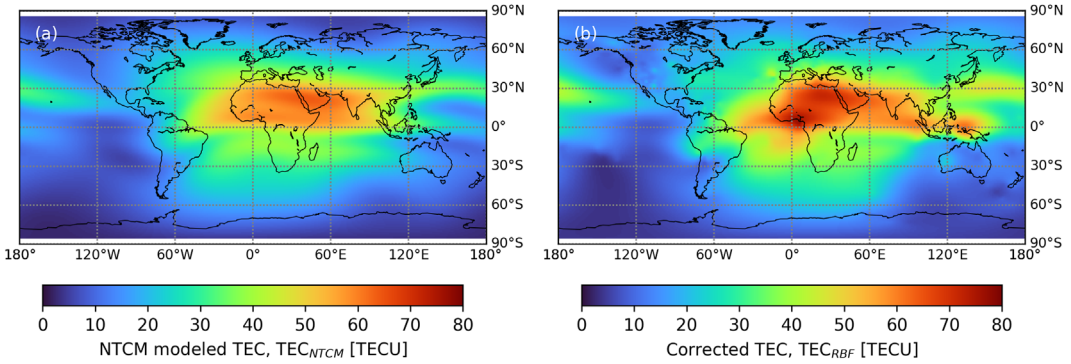

Figure 5. NTCM TEC map (a) and RBF TEC map (b) are shown for 19 May 2023 11:35 UTC.

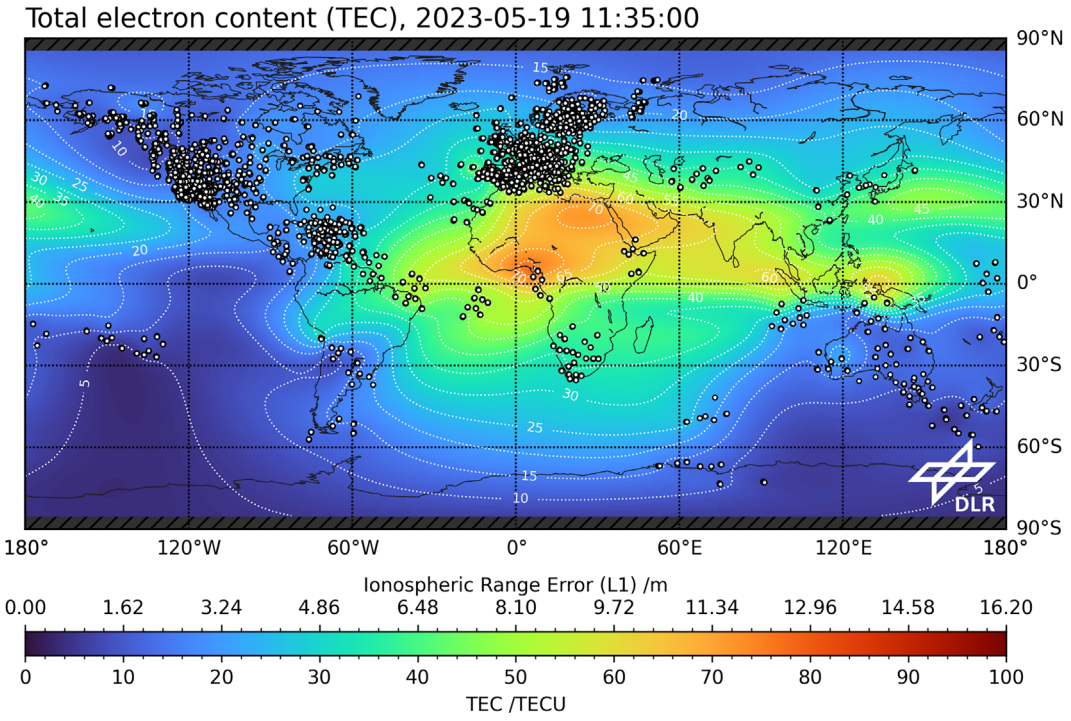

Figure 6. RBF TEC map for 19 May 2023 11:35 UTC. The white dots show the locations of IPP.

4 Validation results

During development of the RBF TEC algorithm, a continuous validation producing automated statistical reports was operated, as exemplified in Figure 8. The report includes the SCM TEC map, the RBF TEC map, and their difference. This allowed us to assess whether the TEC maps fulfill basic expectations. Further, a violin and scatter plot are included to describe the difference with statistical indicators. A scatter plot for the spatial TEC gradients is also included. These gradients are calculated as the second-order accurate central differences at each coordinate c according to

$$\nabla\mathrm{TEC}(c) = \mathrm{TEC}(c+1) - \mathrm{TEC}(c-1). \tag{7}$$

The absolute horizontal TEC gradient is calculated as

$$\nabla\mathrm{TEC} = \sqrt{\nabla\mathrm{TEC}_{\phi}^2 + \nabla\mathrm{TEC}_{\lambda}^2}. \tag{8}$$

The scatter plot in Figure 8e reports a strong correlation (0.96) of both TEC maps, but the scatter plot in Figure 8f shows that the gradients are only moderately correlated (0.64). This reflects the fundamental changes of the method as indicated in Figure 1a. In general, the report cannot answer which TEC map is more appropriate, but it is still a useful tool to monitor the RBF processor and identify possible time periods for detailed validation studies.

Figure 9 shows the correlations of observed TEC at IPP with SCM (a) and RBF (b) TEC to complement the results in Figure 8. The correlation is strong for both results, but $\mathrm{TEC}_{\mathrm{RBF}}$ performs better due to smaller deviations and a significantly better representation of high values. This can be shown by

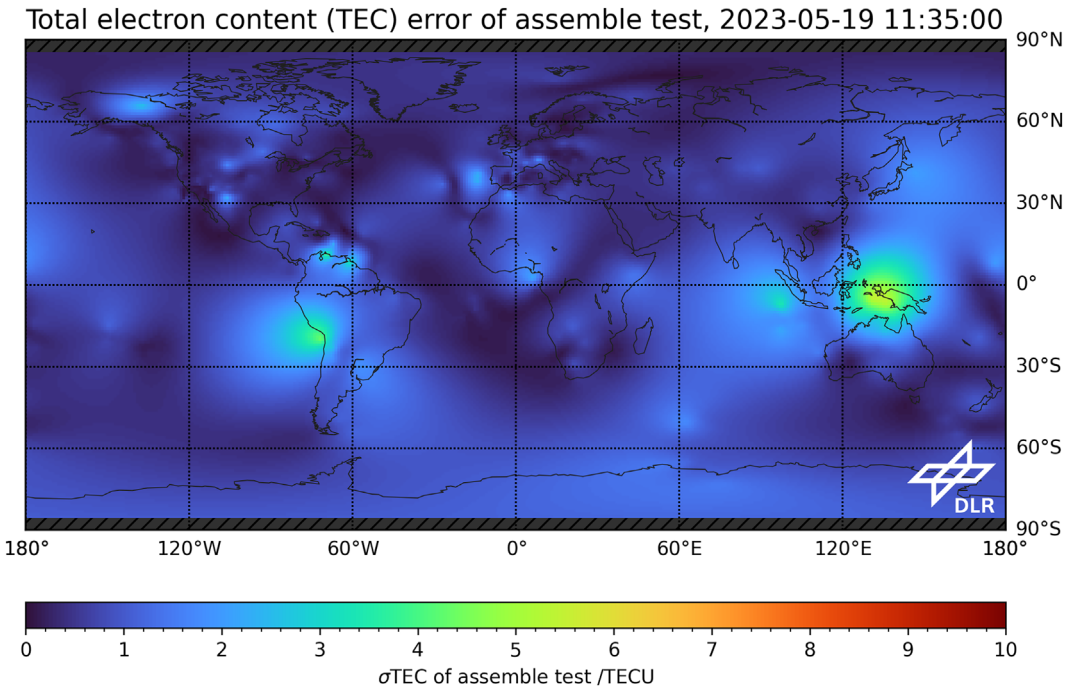

Figure 7. RBF TEC error map for 19 May 2023 11:35 UTC.

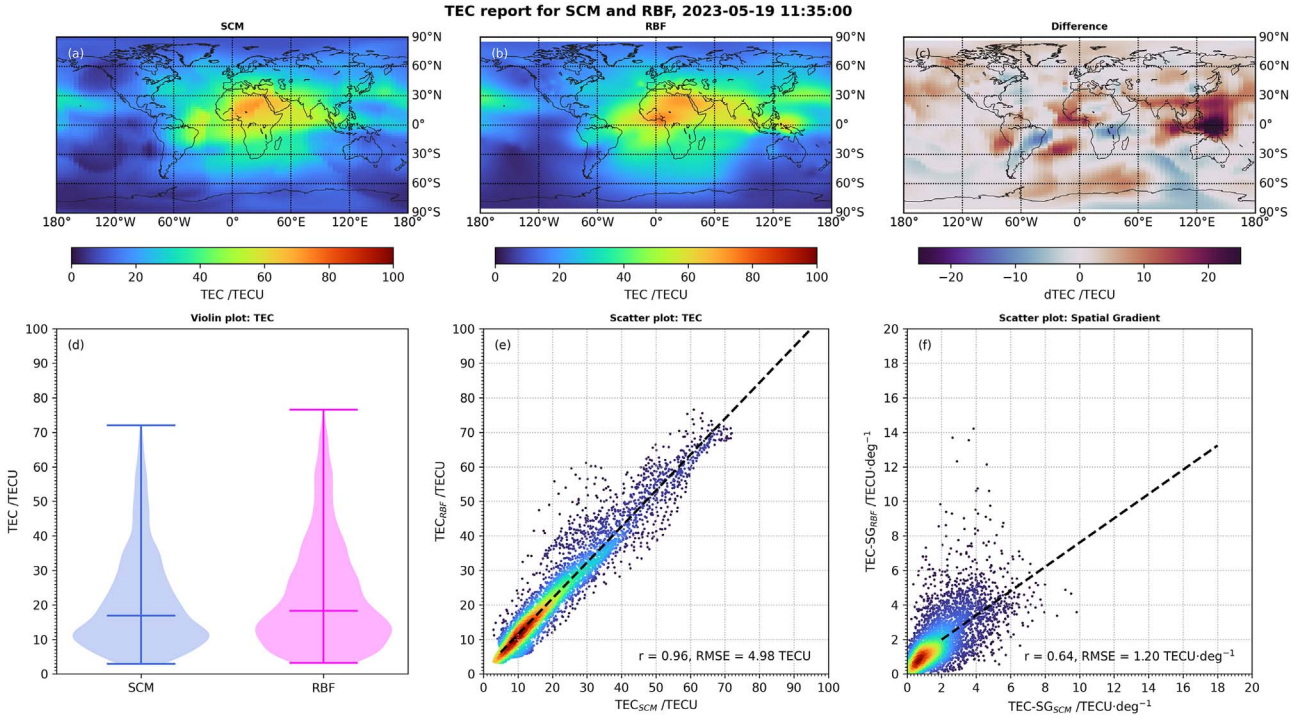

Figure 8. Validation report for 19 May 2023 11:35 UTC. Panels (a) and (b) show the SCM and RBF TEC map. Panel (c) shows the difference between both maps. The distributions are shown with the violin plot (d) and scatter plot (e). Additionally, panel (f) shows the scatter plot for the gradients of both maps.

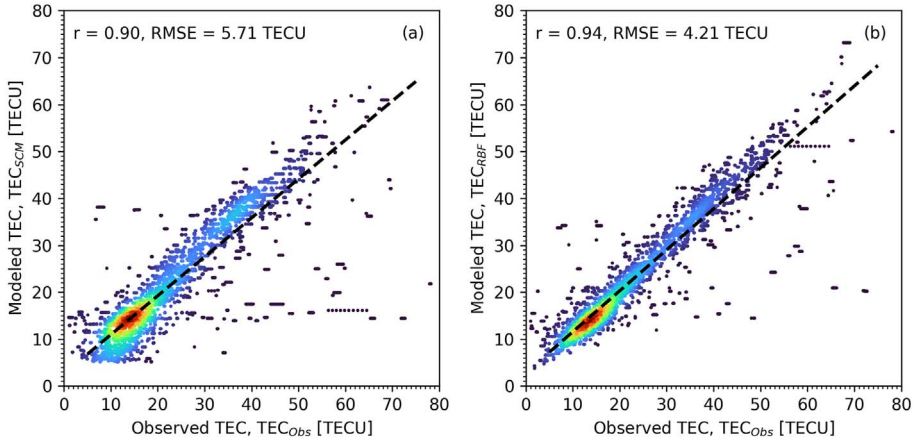

Figure 9. Scatter plots of observed TEC with SCM (a) and RBF (b) TEC for 19 May 2023 11:35 UTC.

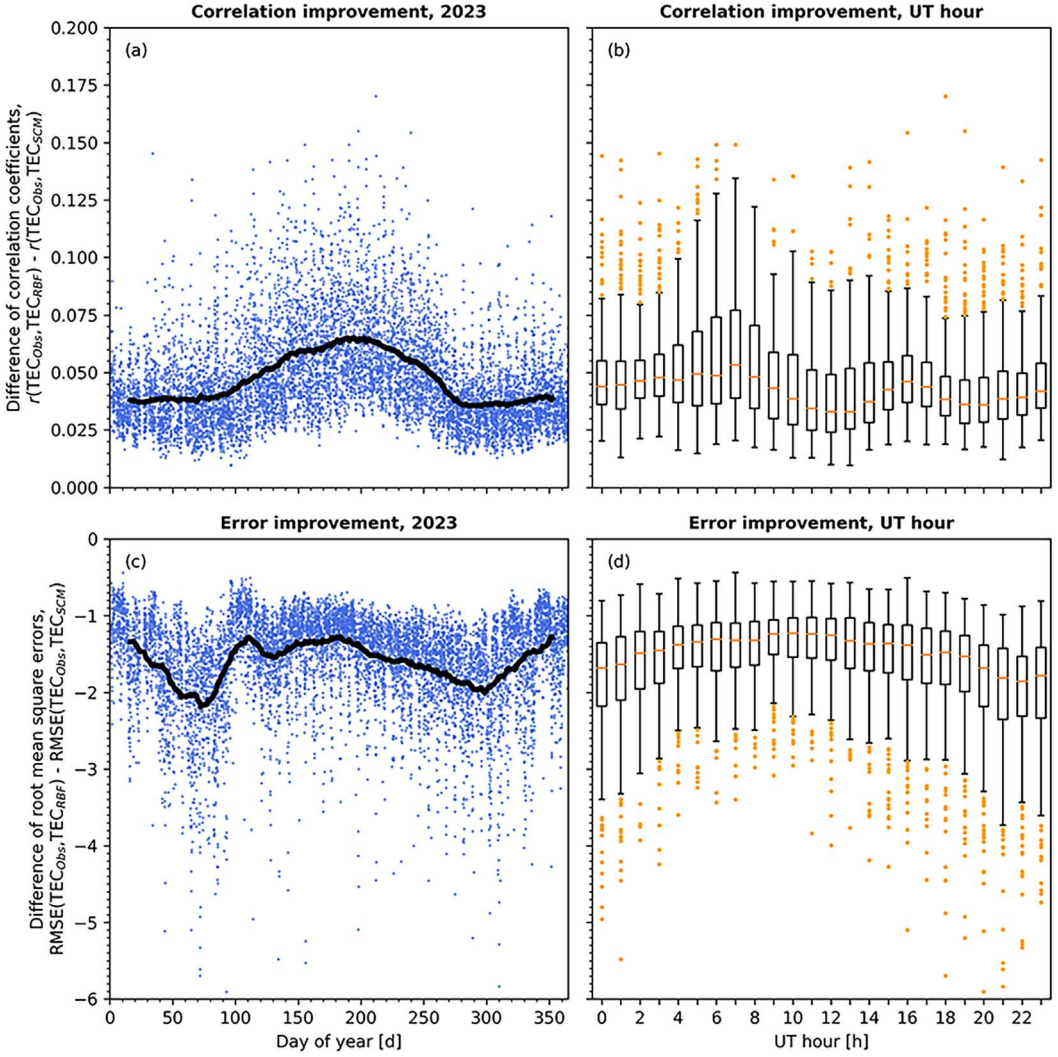

Figure 10. Difference of the correlation coefficients and root mean square errors between RBF TEC and TEC measurements to SCM TEC and TEC measurements is shown in panels (a) and (c) with hourly values and a 27-d running mean (black line) throughout 2023. The distribution of the difference is further summarized with the box plots in panels (b) and (d) for UT hours.

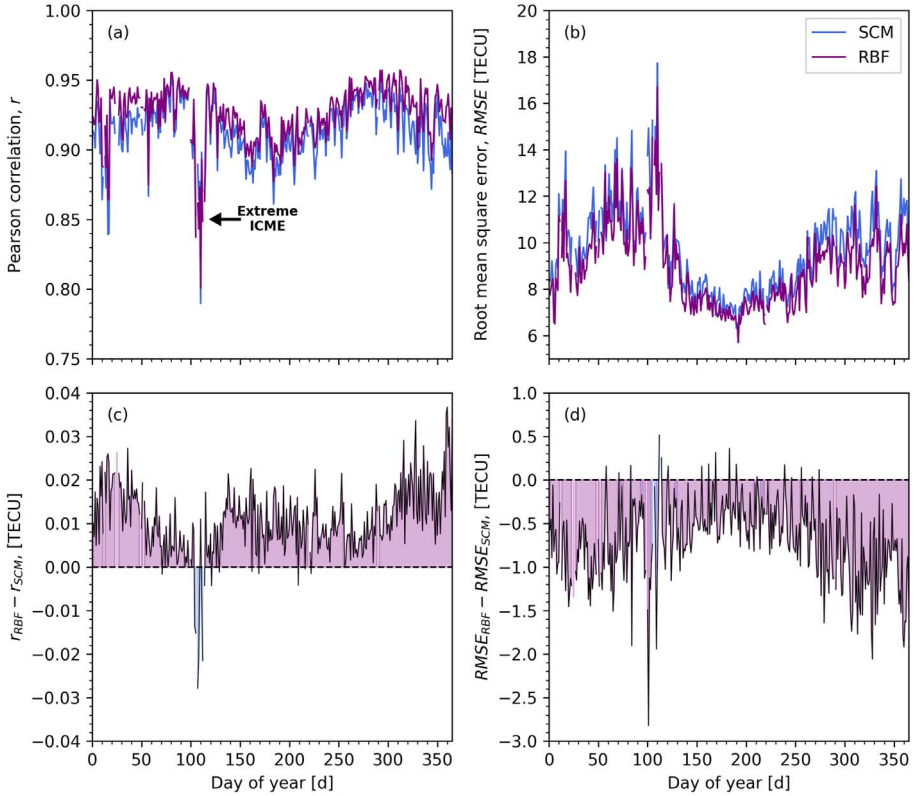

Figure 11. Pearson correlation *r* (a) and root mean square error (*RMSE*) (b) of SCM (blue) and RBF (purple) TEC with UPC TEC for each day in 2023. The differences (c, d) indicate the better-performing data set with the shading in the respective colors.

splitting the values using TEC_{Obs} at 30 TECU. Low values result in correlation coefficients of 0.79 for TEC_{SCM} and 0.87 for TEC_{RBF}. High values result in correlation coefficients of 0.51 for TEC_{SCM} and 0.72 for TEC_{RBF}. Thus, this correlation is improved from moderate to strong.

The comparison of the correlation coefficients of both approaches with the TEC measurements for the entire year 2023 shows a consistent improvement for TEC_{RBF} (see Fig. 10a). The improvement increases in summer months, as the RBF TEC map accounts more reliably for the irregular distribution of measurements in both hemispheres. The distributions of improvements by UT hour in Figure 10b show a strong and weak increase for UT hours 6 and 16, respectively. This corresponds to the times when the ionospheric maximum is observed over East Asia/Australia and the Atlantic, respectively. Thus, TEC_{RBF} performs increasingly better when the maximum TEC values are observed in regions with a lower density of IPP.

The improvement in terms of the root mean square errors (*RMSE*; see Fig. 10c) is a minimum of 0.99 TECU throughout 2023, on average 1.59 TECU (27.78%), and particularly pronounced around the equinoxes. Furthermore, the *RMSE* improves especially between UT hours 19 and 5 (see Fig. 10d). This corresponds to times when the ionospheric maximum is observed over the Pacific. Since this region has an especially low density of IPP (see e.g. Fig. 6), the SCM approach with local fit does not sufficiently adjust the background model. The RBF approach with the global fit, on the other hand, provides adjustments that result in better performance.

Generally, Figure 10 shows that the RBF approach consistently results in improvements of the TEC maps, and this effect is especially significant in time periods or regions with a low number of TEC measurements. Thus, a more detailed investigation of these differences of SCM and RBF TEC maps particularly interesting.

The performance of the RBF TEC map is assessed based on a validation study that covers real-time data from 2023, which compares both the SCM and RBF TEC map against the UPC TEC map. This analysis includes three parts: (1) annual variation of correlation and root mean square error *RMSE*, (2) monthly distribution and *RMSE* maps, as well as (3) applicability for gradient analyses. The RBF approach is considered successful if the RBF TEC map performs similarly to or better than the SCM TEC map for parts 1 and 2 and performs significantly better for part 3.

In preparation for the validation, the SCM and RBF TEC maps are selected or linearly interpolated to the spatial and temporal resolution of the UPC TEC map. Below, correlations, *RMSE* and other statistical indicators are identified with only the SCM and RBF subscript, as UPC is used as a reference in all cases.

4.1 Annual variation of correlation and root mean square error

The Pearson correlation coefficient *r* and *RMSE* for each day in 2023 are summarized in Figure 11. Both data sets are strongly correlated with UPC at any time (mean values of

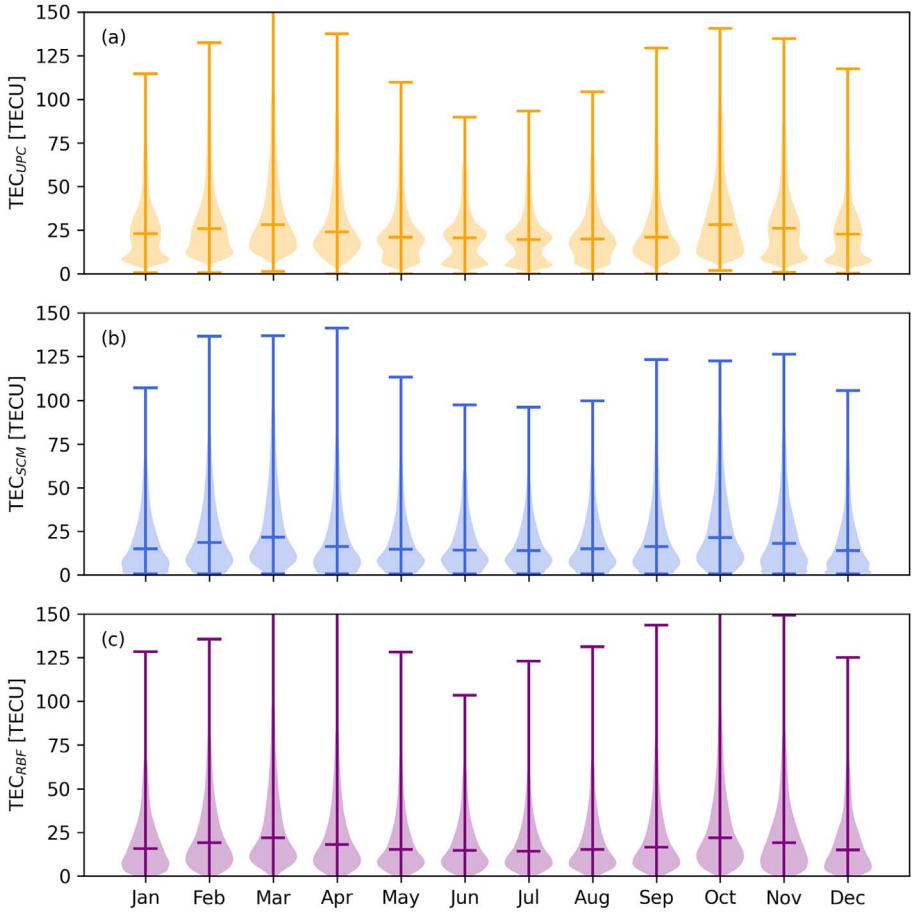

Figure 12. Violin plots for TEC_{UPC} (a), TEC_{SCM} (b), and TEC_{RBF} (c) for each month in 2023 are shown.

0.91 and 0.92), but a strong decrease of the correlations occurs during the 23 April 2023 geomagnetic storm, which was driven by an interplanetary coronal mass ejection (Ghag et al., 2024). The correlation also shows a seasonal variation with an increase during the equinoxes. The cause of this variation should be further investigated in future studies, as a systematic difference to the UPC TEC map is implied. Complex interactions impact the global ionospheric state during the equinoxes (Liu et al., 2010), causing TEC variations, which are reported by various studies for the UPC TEC map (Jerez et al., 2020; Liu et al., 2021a, b). The SCM and RBF TEC maps also appear to be influenced by these processes. Generally, the difference between r_{RBF} and r_{SCM} is small, but except for the strong geomagnetic storm, the RBF TEC map performs better. $RMSE_{RBF}$ and $RMSE_{SCM}$ show the described variations too, and range from approximately 6 to 18 TECU. Thus, no disadvantages for the RBF TEC map are identified in this part of the analysis, and instead, the performance appears to be slightly better.

4.2 Monthly distribution and root mean square error maps

Figure 12 shows the distribution of the three data sets for each month in 2023. The shape of the distribution shows clear differences with consistently unimodal distributions for TEC_{RBF}, but unimodal and bimodal distributions for TEC_{UPC} and TEC_{SCM} during months of higher and lower TEC, respectively. However, the bimodal distribution of TEC_{SCM} is problematic, as these months show very low TEC, resulting in an artificially appearing distribution at 0 TECU (cutoff in model).

Table 1 summarizes statistical indicators for each month. The median values M_{RBF} and M_{SCM} are approximately 6 TECU lower than M_{UPC}, which is significant and has to be further investigated in future studies. As the RBF TEC map is again closer to the UPC TEC map, a small improvement is achieved using the RBF approach. The standard deviations are similar for all three data sets, and r and $RMSE$ indicate a slightly better performance for the RBF TEC map. The number of outliers according to the interquartile range method is also similar for both the SCM and RBF TEC maps, with 4.12% and 4.16%, respectively. Furthermore, the occurrence of outliers does not necessarily have to be a problem if they are introduced by extreme measurements. The interpolation is well-conditioned and provides stable results.

Figures 13 and 14 show the $RMSE$ maps of SCM and RBF for every other month in 2023 (starting with February). These maps show the spatial difference in more detail with pronounced increases at the equatorial crest for the SCM TEC map, which are particularly strong during the equinoxes (see Fig. 13b, e) near the Pacific and Atlantic. These regions have a low density of IPP, and the TEC of the background model

Table 1. Median M, standard deviation σ, Pearson correlation r, and root mean square error (*RMSE*) of TEC_{UPC}, TEC_{SCM}, and TEC_{RBF} for each month in 2023.

Month	M [TECU]			σ [TECU]			r		*RMSE* [TECU]	
	UPC	SCM	RBF	UPC	SCM	RBF	SCM	RBF	SCM	RBF
1	23.10	14.88	15.73	17.58	17.32	17.41	0.90	0.92	10.03	9.21
2	25.70	18.43	18.93	20.90	20.58	20.92	0.92	0.93	10.73	9.86
3	28.20	21.65	21.96	25.12	24.51	25.80	0.93	0.94	11.79	11.05
4	24.00	16.24	17.90	22.00	21.70	22.74	0.90	0.90	12.34	11.63
5	20.90	14.71	15.13	17.19	17.20	18.38	0.91	0.92	8.76	8.22
6	20.70	14.27	14.56	14.66	14.78	15.44	0.90	0.91	7.69	7.30
7	19.70	13.95	14.16	14.24	13.90	14.90	0.89	0.90	7.43	7.07
8	19.90	14.82	15.10	15.84	15.80	16.80	0.91	0.92	7.99	7.55
9	20.90	16.16	16.49	19.41	19.10	20.08	0.93	0.93	8.98	8.39
10	28.10	21.41	21.76	22.66	22.66	23.18	0.93	0.94	10.26	9.43
11	26.00	17.99	18.88	20.93	20.93	21.08	0.92	0.94	10.67	9.53
12	22.60	13.90	14.98	17.72	17.33	17.42	0.91	0.92	10.22	9.18
Mean	23.32	16.53	17.13	19.02	18.82	19.51	0.91	0.92	9.74	9.03

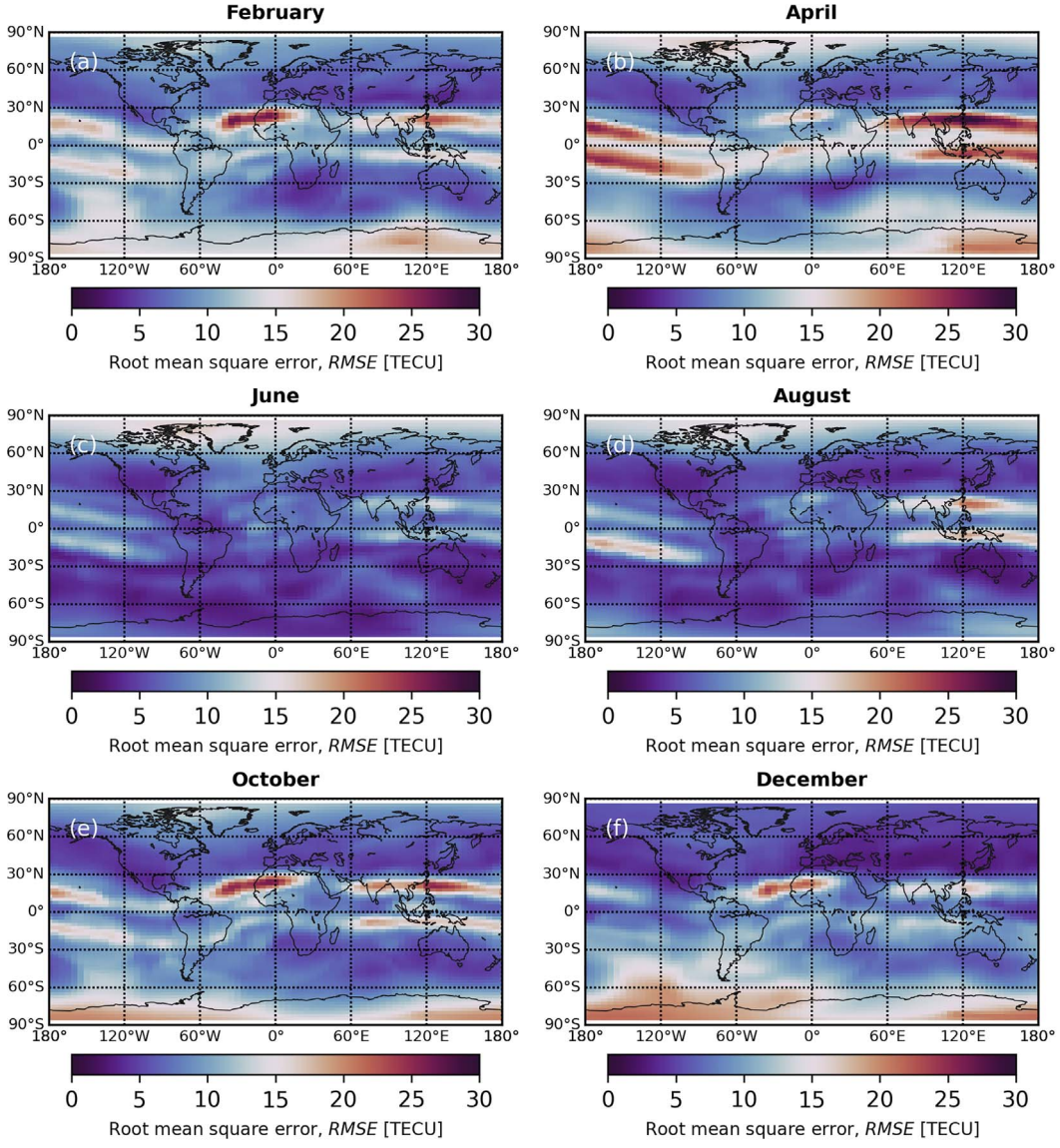

Figure 13. Root mean square error *RMSE* maps of SCM and UPC TEC for six selected months in 2023.

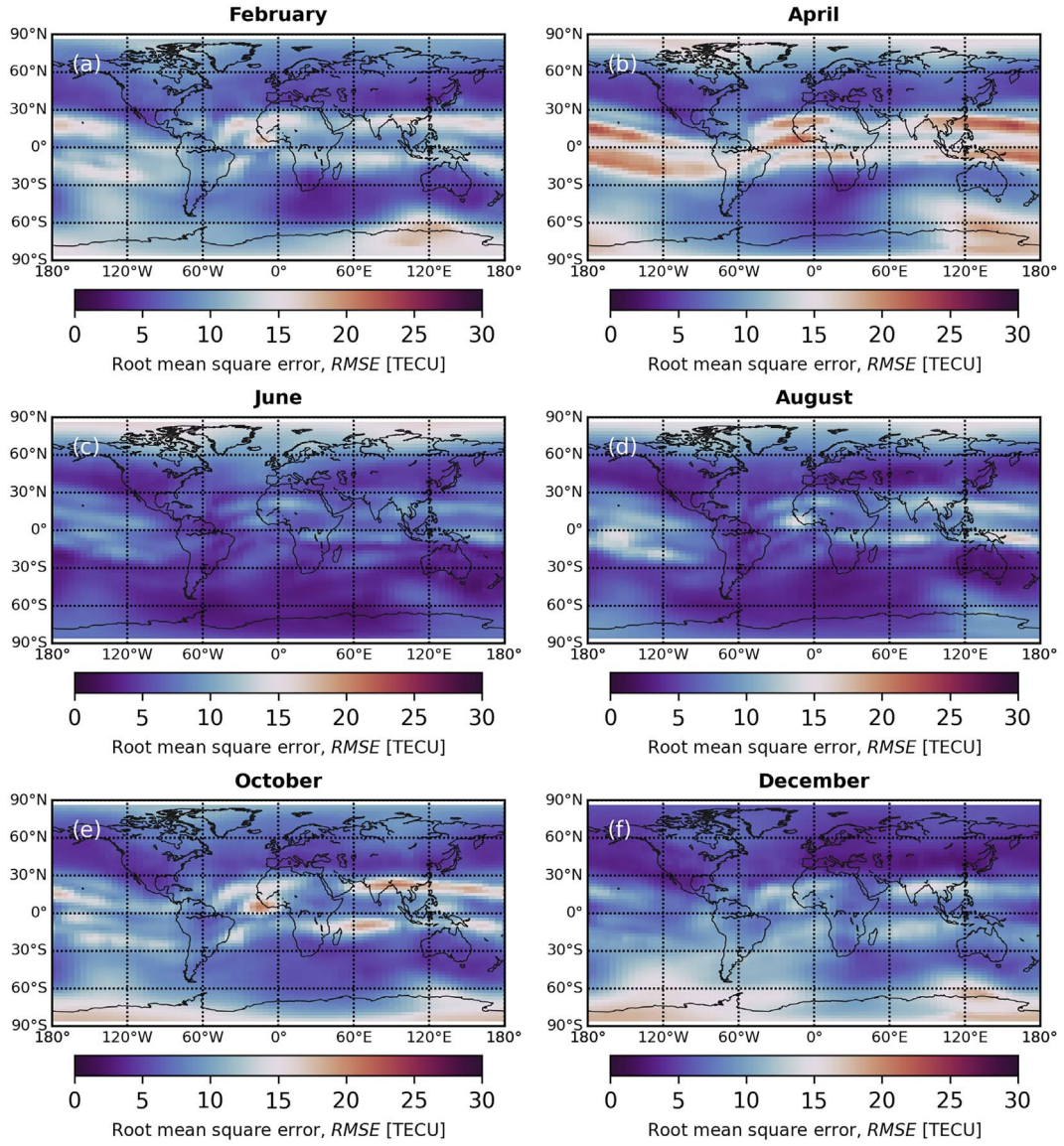

Figure 14. Root mean square error *RMSE* maps of RBF and UPC TEC for six selected months in 2023.

is lower than the measurements, which is not improved by the local fit (see Fig. 1a). Further, increases are observed at high latitudes of the Southern Hemisphere. This is due to the low density of IPP in these regions and likely the shrinking windows of the applied Gaussian kernel (see Fig. 1b).

The increased differences at the equatorial crest are less pronounced for the RBF TEC map, and a significant increase only occurs during the equinox in April (period with the strong geomagnetic storm). The increases at high latitudes of the Southern hemisphere are also less pronounced (especially in October and December), indicating an improvement due to the adjustment in Cartesian coordinates. Generally, the results are satisfactory, but the equatorial crest has to be further investigated in future studies with independent measurements.

Figure 15 summarizes the *RMSE* maps for 00:00, 06:00, 12:00, and 18:00 UT. These results highlight the regional differences more strongly, which is especially noticeable for the equatorial crest along the geomagnetic equator. The performance of the RBF TEC map is significantly better for 06:00 and 12:00 UT over the Pacific and the South Pole, regions with few TEC measurements. The difference at the equatorial crest is also improved for 00:00 and 18:00 UT, though to a smaller extent.

4.3 Applicability for gradient analysis

TEC gradients are of particular interest in regions with high ionospheric activity (e.g., equatorial crest) or during geomagnetic storms for assessing and improving the reliability of navigation services (Arbesser-Rastburg & Jakowski, 2007). Recent studies of space weather impacts in aviation (Schmölter & Berdermann, 2024) highlighted the importance of TEC gradients to describe ionospheric disturbances and motivated the critical review of the SCM TEC map. This study presents TEC gradients according to geographic coordinates in TECU·deg^{-1}

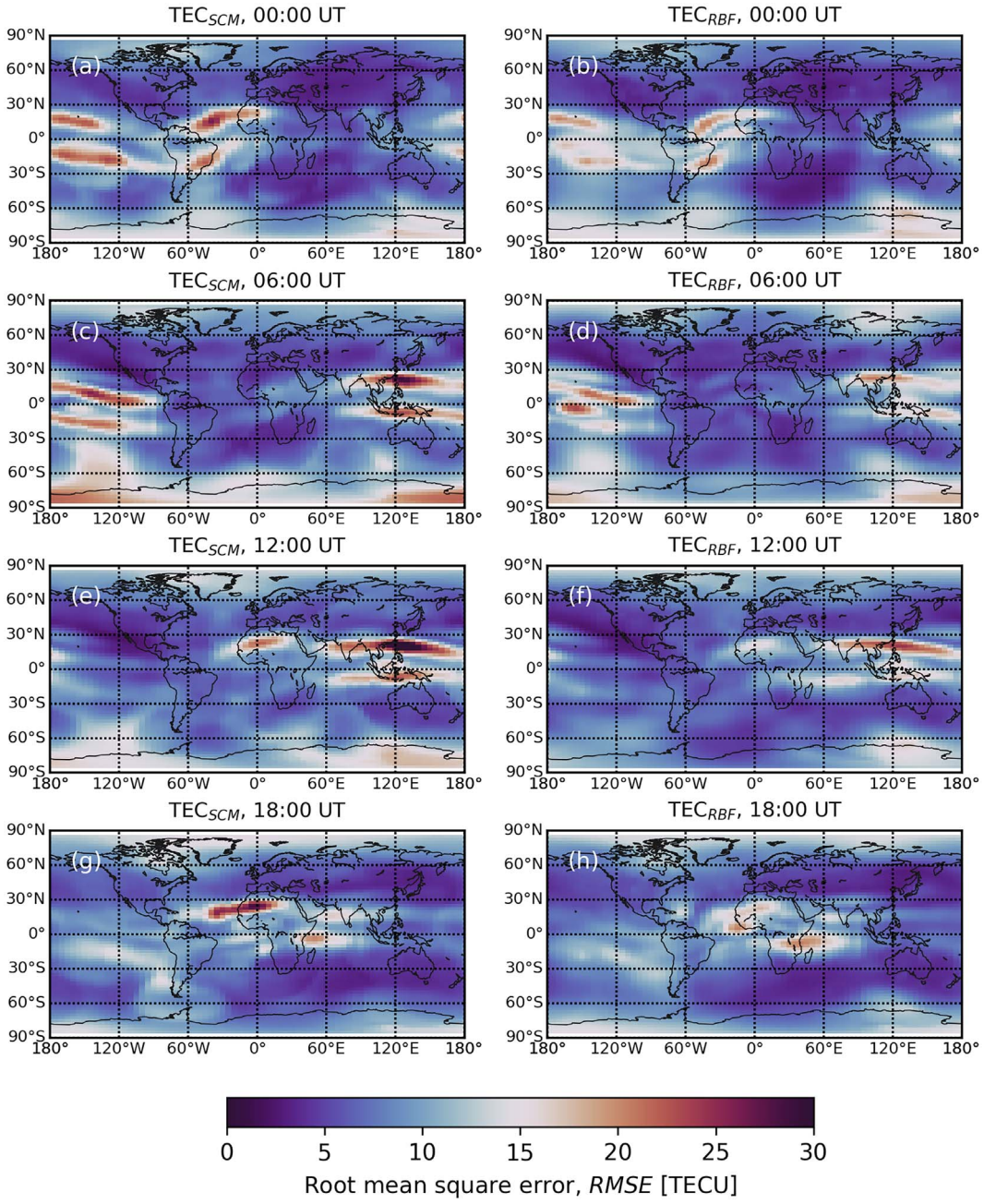

Figure 15. Root mean square error *RMSE* maps of RBF and SCM with UPC TEC for 00:00, 06:00, 12:00 and 18:00 UT.

calculated from the TEC maps (see Eqs. (7) and (8)). These could be converted into distance-dependent values, which would be particularly relevant for applications.

Figure 16 shows the TEC gradients for the SCM and RBF TEC map (see Fig. 8a, b). The remarkably different results may be unexpected considering the strong correlation of both maps (and the similar correlation with the UPC TEC map), but the two processes (see Fig. 1a) superimpose different small-scale variations on the global distribution.

The SCM TEC map (see Fig. 16a) shows noticeable gradients along the equatorial crests with increases towards mid-latitudes and partially at the geomagnetic equator (Western Pacific). This is in good agreement with expectations of the global ionosphere (Balan et al., 2018b), but there are several irregular gradients in the map, that superimpose and even dominate the variability. These gradients occur due to the described transition regions and offsets between measurements and background model (see Figs. 1a and 2). This means that these gradients also exist under varying conditions and complicate statistical analyses or use in applications.

The RBF TEC map (see Fig. 16b) shows the desired improvements with distinct gradients along the equatorial crests and small-scale features limited to regions with measurements. Thus, the global ionosphere is well represented, and

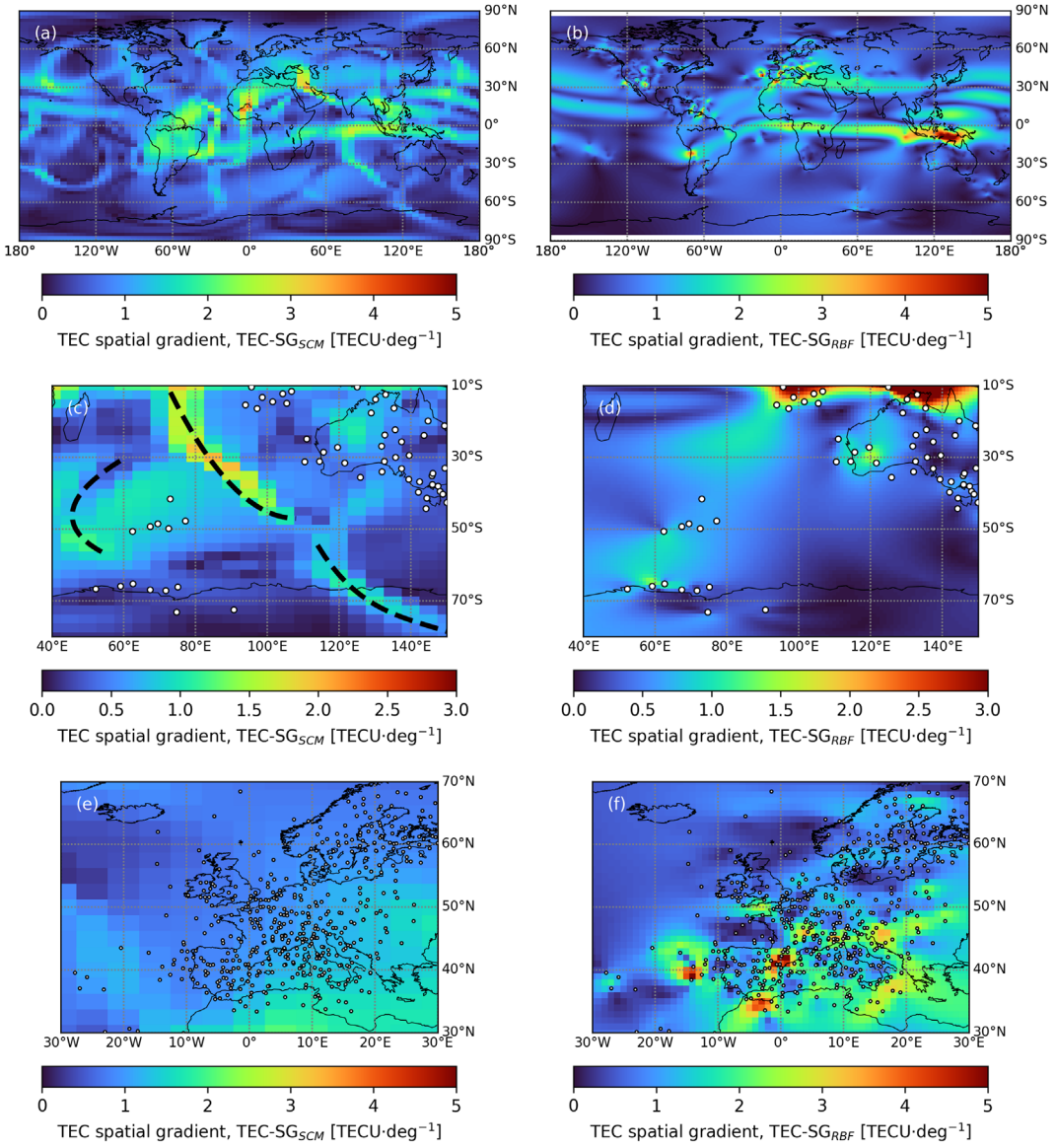

Figure 16. SCM TEC gradient map (a) and RBF TEC gradient map (b) are shown for 19 May 2023 11:35 UTC. The local map of the South Indian Ocean is shown (c, d) as an example for artificial gradients (highlighted with dashed black lines) in the SCM TEC map and the improved representation of that region in the RBF TEC map. The local map of Europe is shown (e, f) to highlight the detailed TEC gradients presented in the RBF TEC map compared to the SCM TEC map. The white dots show the locations of IPP (only first location for each satellite-receiver link).

grid points with strong perturbations can be identified. A simple adjustment of the SCM TEC map, e.g., by applying smoothing filters, would blur or remove both expected and artificial gradients to the same extent. The RBF approach, on the other hand, provides the expected gradients with excellent granularity.

To emphasize this improvement, Figure 16c shows gradients that occur in the SCM TEC map in the South Indian Ocean (traced with dashed lines). The strongest gradient with a maximum of approximately 3.5 TECU·deg^{-1} is centered between Australia and Antarctica (regions with higher density of IPP) and thus located in a transition region as defined in Figures 1a and 2d. Figure 16d shows that, as expected, these gradients do not occur in the RBF TEC map. Although there are still artifacts due to the interpolation (e.g., for isolated IPP), these are insignificant compared to the gradients of ionospheric processes. It is important to note that this "smoothing" by the RBF TEC map only occurs for regions with a low density of IPP. Figures 16e and 16f show the detailed maps for Europe with a high density of IPP. The SCM TEC map averages out several observed gradients due to the insufficient resolution and method. The RBF TEC map, on the other hand, can show detailed variations for these regions due to the higher resolution and RBF method. This is also confirmed by the strong correlation (0.99) between TEC measurements and RBF TEC for this region.

For that reason, the RBF TEC map shows a better performance for all defined requirements of the validation and is appropriate in its default configuration (defined by shell height, type of RBF and smoothing factor).

5 Discussion

Replacing key algorithms in the global TEC map generation of IMPC is a substantial decision and requires reflection on the performance in specific applications (e.g., scientific investigations) and intensive validation. This study presented an RBF algorithm, but more importantly, the validation results were used to investigate those changes that are intended to solve previously identified problems. In the next iteration, after the RBF TEC map has been in use for a longer period of time, further adjustments may be prioritized. This proposed update involves users (e.g., scientist) and allows to address different features over time, as it is not possible to fully test and validate a complex product like TEC maps. Nevertheless, further optimization is intended based on the presented findings.

The main question that arises from this study is how the offset of approximately 6 TECU to UPC can be explained (see Table 1 and Fig. 12). There are various possible causes for this offset, such as differences in the measurements (e.g., network or calibration), background model, assimilation, or a combination of these processes. Future studies should investigate this result in more detail with independent measurements (e.g., peak electron density measurements by the Global-scale measurements of the Limb and Disk mission). The seasonal variation of the correlation and difference (see Fig. 11) may also be explained by such an investigation. Furthermore, the approach could be adapted and optimized with easy-to-implement adjustments. The background model could be changed if a model is available that is generally more appropriate or corresponds more closely to specific requirements of users. The RBF kernel could be changed or the smoothing factor could be adjusted. For the RBF TEC map presented in this study, these parts of the interpolation are configured and optimized manually, which, of course, considerably limits the number of tested combinations. For this reason, automated validation, which uses statistical indicators to identify which parameters are optimized, is desirable for all changes. Initial work for such an automated validation was implemented for the IMPC TEC map, but several processes still must be manually initiated and evaluated.

The advantages of the RBF TEC map according to the validation outweigh possible disadvantages and risks. For that reason, the RBF TEC map will be made available as a space weather product via IMPC (update or alongside the SCM TEC map). A more sophisticated validation should also be implemented along with the operational production to enable long-term monitoring of the performance with low effort.

6 Conclusion

The RBF algorithm presented in this study demonstrates significant improvements compared to the SCM TEC map performance (see Figs. 11, 12, and 14). Especially for the estimation of gradients (see Fig. 16), the RBF TEC map consistently outperforms the SCM TEC map, allowing more reliable and precise space weather monitoring. This in turn also offers an improved tool for decision-making in a variety of applications (e.g., aviation). Future studies should focus on further refining the method and exploring its adaptability across different space weather conditions.

Acknowledgments

We thank IGS for the access to the TEC maps of the different IAAC through CDDIS. The editor thanks two anonymous reviewers for their assistance in evaluating this paper.

Funding

This research did not receive any specific funding.

Conflicts of interest

The authors declare no conflicts of interest.

Data availability statement

UPC TEC maps are available at https://cddis.nasa.gov/archive/gnss/products/ionex/ and IMPC TEC maps are available at https://impc.dlr.de/products.

References

Abdu, MA. 1997. Major phenomena of the equatorial ionosphere-thermosphere system under disturbed conditions. *J Atmos Sol-Terr Phys* **59 (13)**: 1505–1519. https://doi.org/10.1016/s1364-6826(96)00152-6.

Arbesser-Rastburg, B, Jakowski N. 2007. Effects on satellite navigation. *Space Weather Physics and Effects* (1st edn.). Springer Berlin Heidelberg. ISBN 9783540239079. https://doi.org/10.1007/978-3-540-34578-7_13.

Balan, N, Liu L, Le H. 2018a. A brief review of equatorial ionization anomaly and ionospheric irregularities. *Earth Planet Phys* **2 (4)**: 1–19. https://doi.org/10.26464/epp2018025.

Balan, N, Souza J, Bailey GJ. 2018b. Recent developments in the understanding of equatorial ionization anomaly: A review. *J Atmos Sol-Terr Phys* **171**: 3–11. https://doi.org/10.1016/j.jastp.2017.06.020.

Berdermann, J, Kriegel M, Banyś D, Heymann F, Hoque MM, Wilken V, Borries C, Heßelbarth A, Jakowski N. 2018. Ionospheric response to the X9.3 flare on 6 September 2017 and its implication for navigation services over Europe. *Space Weather* **16 (10)**: 1604–1615. https://doi.org/10.1029/2018sw001933.

Blagoveshchensky, DV, Maltseva OA, Sergeeva MA. 2018. Impact of magnetic storms on the global TEC distribution. *Ann Geophys* **36 (4)**: 1057–1071. https://doi.org/10.5194/angeo-36-1057-2018.

Bust, GS, Liles W, Mitchell C. 2021. Space weather influences on HF, UHF, and VHF radio propagation. In: *Space Weather Effects and Applications (1st edn.)* Coster AJ, Erickson PJ, Lanzerotti LJ, Zhang Y, Paxton LJ (Eds.), Geophysical monograph series, Washington, DC, USA, pp. 153–163. ISBN 9781119815570. https://doi.org/10.1002/9781119815570.ch7.

Coster, AJ, Yizengaw E. 2021. GNSS/GPS Degradation from Space Weather. In: *Space Weather Effects and Applications*. Coster AJ, Erickson PJ, Lanzerotti LJ, Zhang Y, Paxton LJ (Eds.), Geophysical monograph series, Wiley, Washington, DC, USA, pp. 165–181. https://doi.org/10.1002/9781119815570.ch8.

Demyanov, V, Yasyukevich Y, Sergeeva MA, Vesnin A. 2022. *Space weather impact on GNSS performance*. Springer International Publishing, Cham, Switzerland. ISBN 9783031158742. https://doi.org/10.1007/978-3-031-15874-2.

Doornbos, E, Klinkrad H. 2006. Modelling of space weather effects on satellite drag. *Adv Space Res* **37 (6)**: 1229–1239. https://doi.org/10.1016/j.asr.2005.04.097.

Fang, T, Kubaryk A, Goldstein D, Li Z, Fuller-Rowell T, Millward G, Singer HJ, Steenburgh R, Westerman S, Babcock E. 2022. Space weather environment during the SpaceX Starlink satellite loss in February 2022. *Space Weather* **20 (11)**: 1–14. https://doi.org/10.1029/2022sw003193.

Fasshauer, GE. 2007. *Meshfree Approximation Methods with Matlab: (With CD-ROM)*. World Scientific, Singapore. ISBN 9789812708632. https://doi.org/10.1142/6437.

Feng, J, Zhang Y, Li W, Han B, Zhao Z, Zhang T, Huang R. 2023.. Analysis of ionospheric TEC response to solar and geomagnetic activities at different solar activity stages. *Adv Space Res* **71 (5)**: 2225–2239. https://doi.org/10.1016/j.asr.2022.10.032.

Flyer, N, Fornberg B, Bayona V, Barnett GA. 2016. On the role of polynomials in RBF-FD approximations: I. Interpolation and accuracy. *J Comput Phys* **321**: 21–38. https://doi.org/10.1016/j.jcp.2016.05.026.

Fornberg, B, Flyer N. 2015. *A primer on radial basis functions with applications to the geosciences*. Society for Industrial and Applied Mathematics, Philadelphia, PA, USA. ISBN 9781611974041. https://doi.org/10.1137/1.9781611974041.

Ghag, K, A Raghav, Bhaskar A, Soni SL, Sathe B, Shaikh Z, Dhamane O, Tari P. 2024. Quasi-planar ICME sheath: A cause of the first two-step extreme geomagnetic storm of the 25th solar cycle observed on 23 April 2023. *Adv Space Res* **73 (12)**: 6288–6297. https://doi.org/10.1016/j.asr.2024.03.011.

Hapgood, M. 2018. Linking space weather science to impacts – the view from the Earth. In:*Extreme Events in Geospace*. Elsevier, Amsterdam, Netherlands. ISBN 9780128127001. https://doi.org/10.1016/b978-0-12-812700-1.00001-7.

Hernández-Pajares, M, Juan JM, Sanz J. 1999. New approaches in global ionospheric determination using ground GPS data. *J Atmos Sol-Terr Phys* **61 (16)**: 1237–1247. https://doi.org/10.1016/s1364-6826(99)00054-1.

Hernández-Pajares, M, Juan JM, Sanz J, Orus R, Garcia-Rigo A, Feltens J, Komjathy A, Schaer SC, Krankowski A. 2009. The IGS VTEC maps: a reliable source of ionospheric information since 1998. *J Geod* **83** (**3–4**): 263–275. https://doi.org/10.1007/s00190-008-0266-1.

Hernández-Pajares, M, Juan JM, Sanz J. 1997. Neural network modeling of the ionospheric electron content at global scale using GPS data. *Radio Sci* **32 (3)**: 1081–1089. https://doi.org/10.1029/97rs00431.

Hoque, MM, Jakowski N, Prol FS. 2022. A new climatological electron density model for supporting space weather services. *J Space Weather Space Clim* **12**: 1. https://doi.org/10.1051/swsc/2021044.

Jakowski, N, Hoque MM, Mayer C. 2011a. A new global TEC model for estimating transionospheric radio wave propagation errors. *J Geod* **85 (12)**: 965–974. https://doi.org/10.1007/s00190-011-0455-1.

Jakowski, N, Mayer C, Hoque MM, Wilken V. 2011b. Total electron content models and their use in ionosphere monitoring. *Radio Sci.* **46 (6)**: 1–11. https://doi.org/10.1029/2010rs004620.

Jančič, M, Slak J, Kosec G. 2021. Monomial augmentation guidelines for RBF-FD from accuracy versus computational time perspective. *J Scientific Comput* **87 (1)**: 1–18. https://doi.org/10.1007/s10915-020-01401-y.

Jerez, GO, Hernández-Pajares M, Prol FS, Alves DBM, Monico JFG. 2020. Assessment of global ionospheric maps performance by means of ionosonde data. *Rem Sens* **12 (20)**: 3452. https://doi.org/10.3390/rs12203452.

Kauristie, K, Andries J, P Beck, Berdermann J, Berghmans D, et al. 2021. Space weather services for civil aviation – challenges and solutions. *Rem Sens* **13 (18)**: 3685. https://doi.org/10.3390/rs13183685.

Kriegel M, Berdermann J. 2020. Ionosphere Monitoring and Prediction Center. In: *2020 European Navigation Conference (ENC)*. IEEE, pp. 1–10. https://doi.org/10.23919/enc48637.2020.9317443.

Krypiak-Gregorczyk, A, P Wielgosz, Jarmolowski W. 2017. A new TEC interpolation method based on the least squares collocation for high accuracy regional ionospheric maps. *Measure Sci Technol* **28 (4)**: 045801. https://doi.org/10.1088/1361-6501/aa58ae.

Liu, L, He M, Yue X, Ning B, Wan W. 2010. Ionosphere around equinoxes during low solar activity. *J Geophys Res Space Phys* **115 (A9)**: 1–10. https://doi.org/10.1029/2010ja015318.

Liu, Q, Hernández-Pajares M, Lyu H, Goss A. 2021a. Influence of temporal resolution on the performance of global ionospheric maps. *J Geod* **95 (3)**: 1–16. https://doi.org/10.1007/s00190-021-01483-y.

Liu, Q, Hernández-Pajares M, Lyu H, Nishioka M, Yang H, et al. 2021b. Ionospheric storm scale index based on high time resolution UPC-IonSAT Global Ionospheric Maps (IsUG). *Space Weather* **19 (11)**: e2021SW002,853. https://doi.org/10.1029/2021sw002853.

Mahbuby, H, Amerian Y. 2021. Regional Assimilation of GPS-Derived TEC into GIMs. *Pure Appl Geophys* **178 (4)**: 1317–1337. https://doi.org/10.1007/s00024-021-02681-7.

Mahbuby, H, Amerian Y. 2022. Improving the performance of time varying spherical radial basis functions in regional VTEC modeling with sparse data. *Adv Space Res* **70 (3)**: 666–686. https://doi.org/10.1016/j.asr.2022.04.067.

Minkwitz, D, Gerzen T, Wilken V, Jakowski N. 2014. Application of SWACI products as ionospheric correction for single-point positioning: a comparative study. *J Geod* **88 (5)**: 463–478. https://doi.org/10.1007/s00190-014-0698-8.

Noll, CE. 2010. The crustal dynamics data information system: A resource to support scientific analysis using space geodesy. *Adv Space Res* **45 (12)**: 1421–1440. https://doi.org/10.1016/j.asr.2010.01.018.

Orús, R, Hernández-Pajares M, Juan JM, Sanz J, Garciía-Fernández M. 2002. Performance of different TEC models to provide GPS ionospheric corrections. *J Atmos Sol-Terr Phys* **64 (18)**: 2055–2062. https://doi.org/10.1016/s1364-6826(02)00224-9.

Orús, R, Hernández-Pajares M, Juan JM, Sanz J, García-Fernández M. 2003. Validation of the GPS TEC maps with TOPEX data. *Adv Space Res* **31 (3)**: 621–627. https://doi.org/10.1016/s0273-1177(03)00026-7.

Roma-Dollase, D, Hernández-Pajares M, Krankowski A, Kotulak K, Ghoddousi-Fard R, et al. 2017. Consistency of seven different GNSS global ionospheric mapping techniques during one solar cycle. *J Geod* **92 (6)**: 691–706. https://doi.org/10.1007/s00190-017-1088-9.

Schmölter, E, and J Berdermann. 2024. Weather- and space-weather-driven variability of ADS-C reports in New Zealand airspace. *IEEE Trans Aerospace Electronic Syst* **60 (6)**: 8034–8053. https://doi.org/10.1109/taes.2024.3423029.

Schmölter, E, Berdermann J, Wilken V, Wenzel D. 2025. Should we monitor space weather effects on surveillance technologies used in air traffic management? First results. *Space Weather* **23 (4)**: e2025SW004,352. https://doi.org/10.1029/2025sw004352.

Sreeja, V. 2016. Impact and mitigation of space weather effects on GNSS receiver performance. *Geosci Lett* **3 (1)**: 1–13. https://doi.org/10.1186/s40562-016-0057-0.

Tariq, MA, Shah M, Hernández-Pajares M, Iqbal T. 2019. Pre-earthquake ionospheric anomalies before three major earthquakes by GPS-TEC and GIM-TEC data during 2015–2017. *Adv Space Res* **63 (7)**: 2088–2099. https://doi.org/10.1016/j.asr.2018.12.028.

Themens, DR, Elvidge S, McCaffrey A, Jayachandran PT, Coster A, et al. 2024. The high latitude ionospheric response to the major May 2024 Geomagnetic Storm: A synoptic view. *Geophys Res Lett* **51 (19)**: 1–11. https://doi.org/10.1029/2024gl111677.

Virtanen, P, Gommers R, Oliphant TE, Haberland M, Reddy T, et al. 2020. SciPy 1.0: fundamental algorithms for scientific computing in Python. *Nature Methods* **17 (3)**: 261–272. https://doi.org/10.1038/s41592-019-0686-2.

Wahba, G 1990. *Spline Models for Observational Data*. Society for Industrial and Applied Mathematics, Philadelphia, PA, USA. ISBN 9781611970128. https://doi.org/10.1137/1.9781611970128.

Cite this article as: Schmölter E, Tagargouste Y, Wilken V, Kriegel M & Berdermann J, 2025. Improving the global Total Electron Content maps provided by the Ionosphere Monitoring and Prediction Center – preliminary results. *J. Space Weather Space Clim.* **15**, 44. https://doi.org/10.1051/swsc/2025039.